*materials proceedings*

MDPI

*Proceeding Paper*

# Uniaxial Tensile Testing of the Native Porcine Pericardium †

**Edward Matjeka [1], Alex G. Kuchumov [2,3], Harry M. Ngwangwa [1], Thanyani Pandelani [1,*] and Fulufhelo Nemavhola [4]**

[1] Department of Mechanical, Bioresources and Biomedical Engineering, University of South Africa, Pretoria 0002, South Africa; 47678534@mylife.unisa.ac.za (E.M.); ngwanhm@unisa.ac.za (H.M.N.)
[2] Research Center for Genetics and Life Sciences, Sirius University of Science and Technology, 354340 Sirius, Russia; kychymov@inbox.ru
[3] Biofluids Laboratory, Perm National Research Polytechnic University, 614990 Perm, Russia
[4] Department of Mechanical Engineering, Faculty of Engineering and the Built Environment, Durban University of Durban, Durban 4001, South Africa; fulufhelon1@dut.ac.za
* Correspondence: epandet@unisa.ac.za
† Presented at the 4th International Conference on Applied Research and Engineering, Pretoria, South Africa, 21–23 November 2025.

**Abstract**

Death rates related to heart failure amount to approximately 50% of deaths globally, and one of the leading causes of heart failure is aortic valve failure, which is treated using prosthetic aortic valves. Porcine pericardium is amongst the materials used to develop a potentially ideal bioprosthetic aortic valve. The mechanical properties of native porcine pericardium are necessary for enhancing a prosthetic aortic valve. The aim of this study was to determine the mechanical properties of porcine pericardium and find optimized material parameters for finite element analysis using five isotropic models. Uniaxial rupture tests were performed using Cellscale biotester to measure the force at rupture, stiffness, and deformation at rupture. Tests were done in circumferential and radial directions, and one-way Anova was used to evaluate different behaviors in both directions. The average coefficient of determination was used to find the model that performed better.

**Keywords:** bioprosthetic aortic valve; pericardium; stenosis; regurgitation

## 1. Introduction

Patients who lose their lives due to heart failure worldwide are commonly affected by valvular diseases and, more commonly, aortic valve stenosis and regurgitation [1]; these failures are common in patients older than 50 years [2]. The aortic valve failures associated with newborn babies are congenital bicuspid valves, where babies have two leaflets on their aortic valves, and this can have an impact on the amount of blood supplied to the entire body [3]. The best way to diagnose patients with aortic valve failure is by implanting a prosthetic aortic valve either surgically or using the transcatheter implantation method [4]. The prosthetic heart valves used are mechanical, bioprosthetic, polymeric, and tissue-engineered. The downsides of these valves are inferior hemodynamics, durability, and somatic growth, respectively. Somatic growth is an issue for all three valves [5]. Tissue-engineered valves are developed to address issues associated with the valves mentioned above, although their downside is that they rely on the patient's regeneration rate, which makes them patient-specific [6]. Material parameters are necessary to material and design a valve according to the patient's requirements. Material optimization for manufacturing is an ongoing process that improves the durability and life cycle of manufactured components [7].

Check for updates

Academic Editor: Tiyamike Ngonda

Published: 28 April 2026

**Copyright:** © 2026 by the authors. Licensee MDPI, Basel, Switzerland. This article is an open access article distributed under the terms and conditions of the Creative Commons Attribution (CC BY) license.

Fiber enhancement and development are among the important factors that help develop desired prosthetic aortic valves [8]. Health is among the leading factors to consider when designing and manufacturing systems and components [9].

Landrace pig's pericardia are used to develop bioprosthetic aortic valves with limited understanding of their mechanical properties [10]. A proper understanding of their mechanical properties would help with the development of an ideal prosthetic aortic valve [11,12], help with diagnosing patients, and facilitate the development of a robust simulation model that predicts valve behavior under different conditions [13]. Finite elements analysis (FEA) would be performed by embedding obtained material parameters into a commercial FEA software constitutive model that is readily available or by using subroutines that allow users to use their own constitutive law to define the material [14]. A comparison of experimental results to simulated results would validate the usage of material parameters [15] for fluid–structure interaction. The aim of this study was to evaluate rupture load, deformation at rupture, and the Young's modulus when subjected to uniaxial loading in the Ref. [6] circumferential and radial direction by using one axis of the Cellscale biotester [16]. Material parameters were optimized by using a Genetic algorithm and five isotropic constitutive models—the Ogden, Klosner–Segal, Arruda–Boyce, Van de Waals, and Yeoh models [17]. Anisotropic constitutive models that are currently available were derived by looking at the microstructural orientation of tissues like arteries and tendons, and those models have both the anisotropic and isotropic parts representing their strain energy function. Since porcine pericardium does not have a strain energy function that was specifically derived from it, it was found to be necessary to assess the ability of five isotropic models to predict stress and strain responses of porcine pericardium when subjected to uniaxial tensile testing. Uniaxial tensile tests are necessary to independently assess a material's response in one direction [18], which supports our decision to select isotropic models to predict material responses. Even though the material undergoes biaxial loading, it is necessary to find its uniaxial response as it is fundamental to properly characterizing a material, as a material behaves differently under different loading conditions [19]. These results are necessary for finite element analysis. Uniaxial testing alone is not enough to characterize soft tissue, as it is complemented by biaxial and shear or bending tests [20].

## 2. Material and Methods

Fresh hearts of fifty-one-week-old landrace pigs with a weight interval of 100 kg to 110 kg were purchased from a local abattoir. Immediately after slathering, a total of six hearts were taken to a biomedical engineering laboratory located approximately 10 km away from the abattoir. An ice-cold box was used to transport the landrace pig hearts from the abattoir to the laboratory. Landrace pig hearts with pericardium collected from the abattoir and the cooler box containing the specimens are shown in Figure 1a,b.



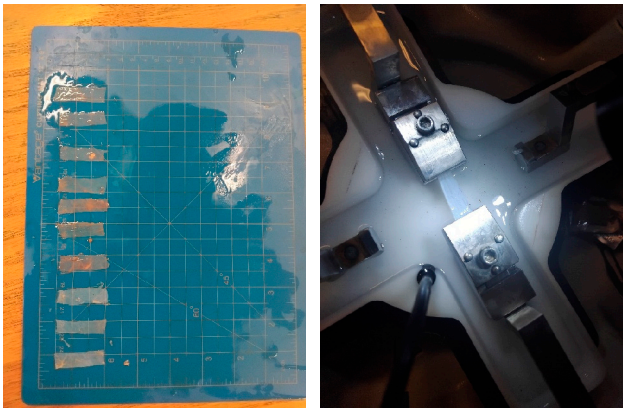
(**a**) (**b**)

**Figure 1.** (**a**) Heart with pericardium intact. (**b**) Ice cooler box with landrace pig heart samples collected from a local abattoir.

https://doi.org/10.3390/materproc2026031023

The samples were removed one at a time to remove the porcine pericardium and cut to the specified dimensions using twizzles, scalpels, and blades. To accurately cut the pericardium into the right sizes, a measurement-sized cutting board was used, and to measure the thickness of the samples, a Vanier caliper was used. The circumferential and radial directions of the specimen were found by cutting the horizontal from the apex and perpendicular direction of the pericardium, respectively.

The hearts of landrace pigs with intact pericardium were collected from a local abattoir that is approximately 15 min from the laboratory. To preserve the material and prevent degradation, a cooler box of ice was used to carry the hearts. Upon their arrival at the laboratory, 40 mm × 10 mm pericardium sizes were dissected from each of the six hearts collected from the abattoir, and the samples were taken from arbitrary regions of the pericardium of the heart. Six samples were chosen because of the porcine pericardium stress and strain responses that are closely related to different regions of the pericardium. An axis of a cellscale biaxial biotester machine was used to perform a uniaxial test, where the fluid chamber was filled with phosphate-buffered saline (PBS) and the temperature was maintained at 37 °C to mimic physiological conditions. PBS allows the material to maintain its mechanical properties and respond the same way it would under physiological loading conditions and cyclic loading, as is the case when it is implanted in the body [21]. Two clamping devices were used to hold the samples on both sides, with each clamp gripping 10 mm, and the free length of the samples was 20 mm. Figures 2a and 2b show the specimens cut to size and mounted to the Cellscale biotester, respectively.



(**a**) (**b**)

**Figure 2.** (**a**) Samples cut into sizes of 40 mm × 10 mm. (**b**) Sample mounted to the CellScale biotester using clamps.

### *2.1. Constitutive Models*

Deformation gradient:

$$F = \begin{bmatrix} \lambda_1 & 0 & 0 \\ 0 & \lambda_2 & 0 \\ 0 & 0 & \lambda_3 \end{bmatrix} \quad (1)$$

where $\lambda_1, \lambda_2$ and $\lambda_3$ are the principal stretches.

The Right-Cauchy–Green tensor:

$$C = F^T F \quad (2)$$

First and second invariants $I_1$, $I_2$, respectively, denoted from the right Cauchy–Green tensor.

$$I_1 = tr(C) = \lambda_1^2 + \lambda_2^2 + \lambda_3^2 \quad (3)$$

$$I_2 = \frac{1}{2}\left(tr(C))^2 - tr\left(C^2\right)\right) = \lambda_1^2\lambda_2^2 + \lambda_1^2\lambda_3^2 + \lambda_2^2\lambda_3^2 \quad (4)$$

#### 2.1.1. Material Models

Five material models, which are hyperelastic and defined by the principal stretches and the first and second invariants, were chosen for this study. The chosen models are the Klosner–Segal model, the Ogden model, the Yeoh model, the Aruda–Boyce model, and the Van de Waals model. Three isotropic models—Klosner–Segal, Aruda–Boyce, and Van de Waals—have not yet been used to capture the isotropic behavior of porcine pericardium, which led to this study evaluating two popularly used isotropic models and three rarely used models. The Klosner–Segal model was derived to capture large strains and effectively capture transitions from different faces of deformations. The model uses two invariants with four material parameters [22]. Partial derivatives of the strain energy with respect to the first and second invariants are taken to obtain the Cauchy stress. The Ogden model strain energy is defined by principal stretches, and the principal uniaxial Cauchy stress is obtained by taking the derivative of the strain energy with respect to the principal stretches [23]. The Yeoh model is based on the first invariant, and to find the Cauchy stress, a strain energy derivative with respect to the first invariant is taken [11]. The Yeoh model order term is optional, and the most commonly used one is the third-order model, which was used in this study. The Arruda–Boyce strain energy is based on the first invariant, and the Cauchy stress is derived by taking the derivative of the strain energy with respect to the first invariant [14]. The Van de Waals strain energy is based on the first deviatoric invariant, and the Cauchy stress is derived from taking the derivative of the strain energy with respect to the first deviatoric invariant [24].

Klosner–Segal

The Klosner–Segal strain energy density is given as follows [12].

$$\Psi = C_{11}(I_1 - 3) + C_{21}(I_2 - 3) + C_{22}(I_2 - 3)^2 + C_{23}(I_2 - 3)^3 \quad (5)$$

where $C_{11}$ and $C_{21}$ represent linear shear stiffness and linear network stiffness, respectively, and are both related to the initial shear modulus, and $C_{22}$ and $C_{23}$ are the non-linear strain stiffening coefficients.

The initial shear modulus is denoted as follows.

$$\mu_0 = 2(C_{11} + C_{21}) \quad (6)$$

Cauchy stress

$$\sigma = 2\left[\frac{\partial\psi}{\partial I_1} + I_1\frac{\partial\psi}{\partial I_2}\right]b - 2\frac{\partial\psi}{\partial I_2}b^2 \quad (7)$$

$$\sigma = 2\left[C_{11} + I_1\left\{C_{21} + 2C_{22}(I_2 - 3) + 2C_{23}(I_2 - 3)^2\right\}\right]b - 2\left[C_{21} + 2C_{22}(I_2 - 3) + 2C_{23}(I_2 - 3)^2\right]b^2 \quad (8)$$

Ogden Model

The Ogden strain energy density for incompressible material is given as follows [23].

$$\Psi = \sum_{i=1}^{N}\frac{\mu_i}{\alpha_i}(\lambda_1^{\alpha_i} + \lambda_2^{\alpha_i} + \lambda_3^{\alpha_i} - 3) \quad (9)$$

where $\mu_i$ and $\alpha_i$ are material parameters with $\mu_i$ having the same units as stress; $N$ is the order term of the model; and $\alpha_i$ is dimensionless.

https://doi.org/10.3390/materproc2026031023

The initial shear modulus is denoted as follows.

$$\mu_0 = \sum_{i=1}^{N} \frac{\mu_i \alpha_i}{2} \tag{10}$$

Principal Cauchy stress

$$\sigma_i = \lambda_i \frac{\partial \psi}{\partial \lambda_i} = \sum_{i=1}^{N} \mu_i (\lambda_i^{\alpha_i}) \tag{11}$$

Yeoh Model

The Yeoh strain energy density is given as follows [25].

$$\Psi = C_{10}(I_1 - 3) + C_{20}(I_1 - 3)^2 + C_{30}(I_1 - 3)^3 \tag{12}$$

where $C_{10}$ represents the material parameters with Pascal's units, which are related to the initial shear modulus, and $C_{20}$ and $C_{30}$ are responsible for capturing strain stiffening at higher strains [17].

The initial shear modulus is denoted as follows.

$$\mu_0 = 2C_{10} \tag{13}$$

Cauchy stress

$$\sigma = \frac{2}{J}\left(\frac{\partial \psi}{\partial I}\right) b = \frac{2}{J}[C_{10} + 2C_{20}(I_1 - 3) + 3C_{30}I_1 - 3)^2]b \tag{14}$$

where $J$ is the volume change and is equal to one for incompressible material; $b$ is the left Cauchy strain tensor, denoted as follows.

$$b = FF^T \tag{15}$$

Arruda–Boyce Model

The Arruda–Boyce strain energy density is given as follows [26].

$$\Psi = \mu \sum_{i=1}^{5} \frac{C_i}{\lambda_L^{2i-2}} (I_1^i - 3^i) \tag{16}$$

Cauchy stress

$$\sigma = \frac{2}{J}\left(\frac{\partial \psi}{\partial I}\right) b = \frac{2}{J}(\mu \sum_{i=1}^{5} \frac{C_i}{\lambda_L^{2i-2}} I_1^{i-1})b \tag{17}$$

where $\mu$ is the shear modulus, $\lambda_L$ is the maximum stretch that the material can undergo, and $C_i$ represents series expansion of the inverse Langevin function.

Van der Waals Model

The Van der Waals strain energy density is given as follows [24].

$$\Psi = \mu\{-\left({\lambda_L}^2 - 3\right)[ln(1-\eta) + \eta] - \frac{2}{3}a\left(\frac{\overline{I}_1 - 3}{2}\right)^{\frac{3}{2}}\} \tag{18}$$

where $\eta = \sqrt{\frac{\bar{I}_1 - 3}{\lambda_L{}^2 - 3}}$, $\bar{I}_1$ is the deviatoric strain invariant given by $\bar{I}_1 = J^{-2/3} I_1$, $\mu$ is the initial shear modulus, $\lambda_L$ is the maximum stretch that the material can undergo, and $\alpha$ is another essential material parameter controlling the rounding and flattening.

Cauchy stress

$$\sigma = \frac{2}{J}\left(\frac{\partial \psi}{\partial \bar{I}_1}\right) dev[\bar{b}] \tag{19}$$

$$\sigma = \mu\left[\frac{1}{1-\eta} - \alpha\sqrt{\frac{\bar{I}_1 - 3}{2}}\right] dev[\bar{b}] \tag{20}$$

Genetic algorithm

Hyperfit software was used to find the optimum material parameters. The genetic algorithm was found to be suitable to use as an optimizer for finding optimized material parameters because of its ability to not get stuck in the local or global minima. The measuring tools to use for selecting an optimized constitutive model with optimum parameters are the sum of squares of errors, sum of absolute errors, normalized errors, normalized root mean squared errors, coefficient of correlation, and coefficient of determination. Constitutive models were used to fit experimental data by initializing material parameters and reducing error terms that include the aforementioned and the coefficient of determination, where 1000 iterations were set for optimum material parameters.

## 3. Results

*Uniaxial Tensile Tests*

The homogeneity of variance assumption was verified prior to one-way ANOVA analysis. Uniaxial results in the circumferential and radial directions are shown in Figure 3, where the stress and strain graphical representation in the circumferential direction are compared to those in the radial direction. Statistical significance was observed when comparing the induced strain in the circumferential direction 0.2699083 ± 0.084227 to the radial direction 0.5692333 ± 0.121948 ($p$ = 0.000581). The maximum stress at rupture or applied to the sample has statistical significance in the circumferential direction 11.6695 ± 0.329884 compared to the radial direction 8.569167 ± 1.808626 ($p$ = 0.003656). The results obtained suggest that the radial direction is more compatible with the applied stress and rupture at an average stress of 8.569167 ± 1.808626 MPa, which is not the case for the circumferential direction, in which the maximum applied stress could not fracture the samples. Young's modulus in the circumferential direction 61.186742 ± 12.351925 MPa is statistically significant compared to Young's modulus in the radial direction 33.100233 ± 10.032143 MPa ($p$ = 0.001505). The material response for both the radial and circumferential directions did not show significant variability.

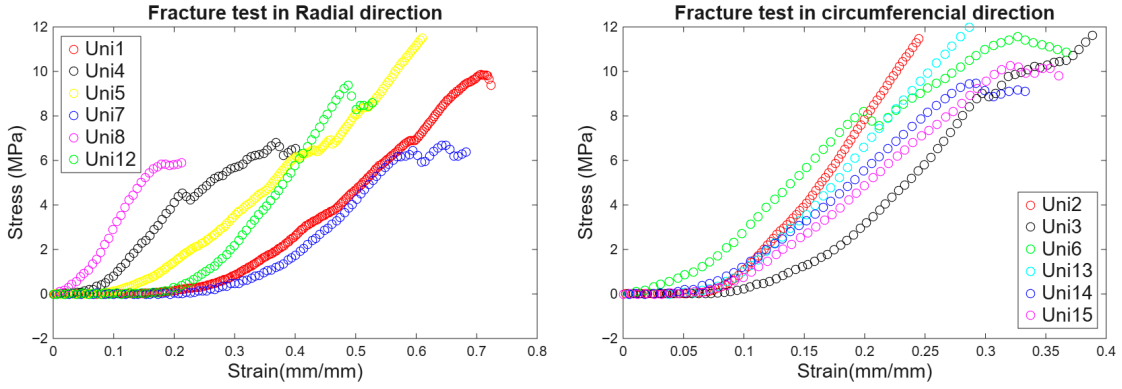



**Figure 3.** Uniaxial test results in the circumferential and radial directions.

The performance of five chosen isotropic constitutive models was evaluated by comparing the coefficients of determination and error terms mentioned above. The average material parameters and optimizing parameters like the coefficients of determination, correlation coefficients, normalized root mean squared error, normalized error, sum of squares of differences, and sum of absolute differences were used to find the optimum constitutive model from the selected model.

A graphical depiction showing the fitting of the chosen constitutive model to the experimental data is shown in Figure 2. After using each experimental data to find material parameters and taking the average of those parameters and the average experimental results, average material parameters for each model were fitted to the average experimental data to evaluate their performance on average data, and the results are shown in Figure 4.

The averaged material parameters obtained from curve fitting using five isotropic models and the genetic algorithm from Hyperfit are given in Tables 1 and 2 below.

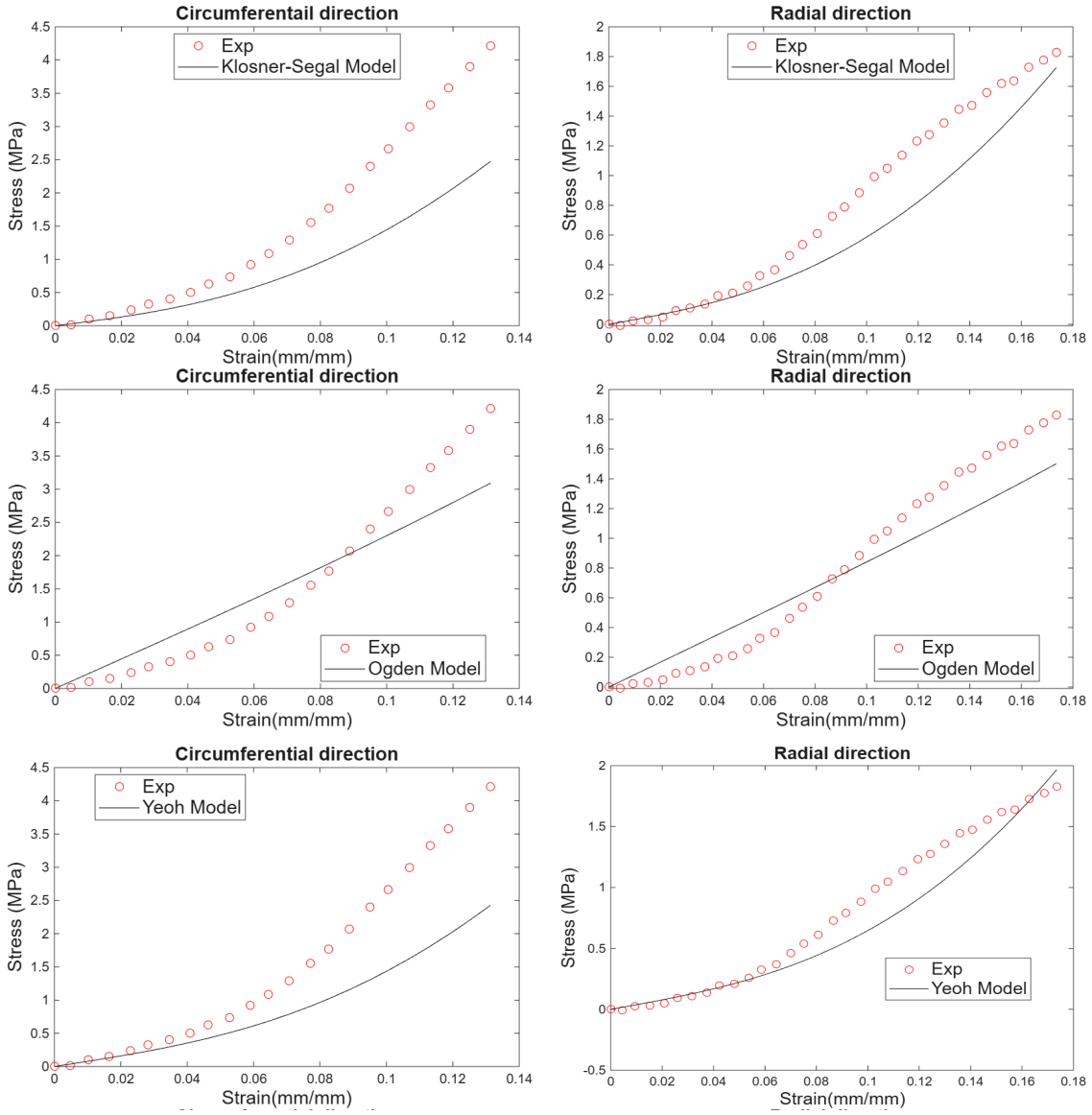



**Figure 4.** *Cont.*

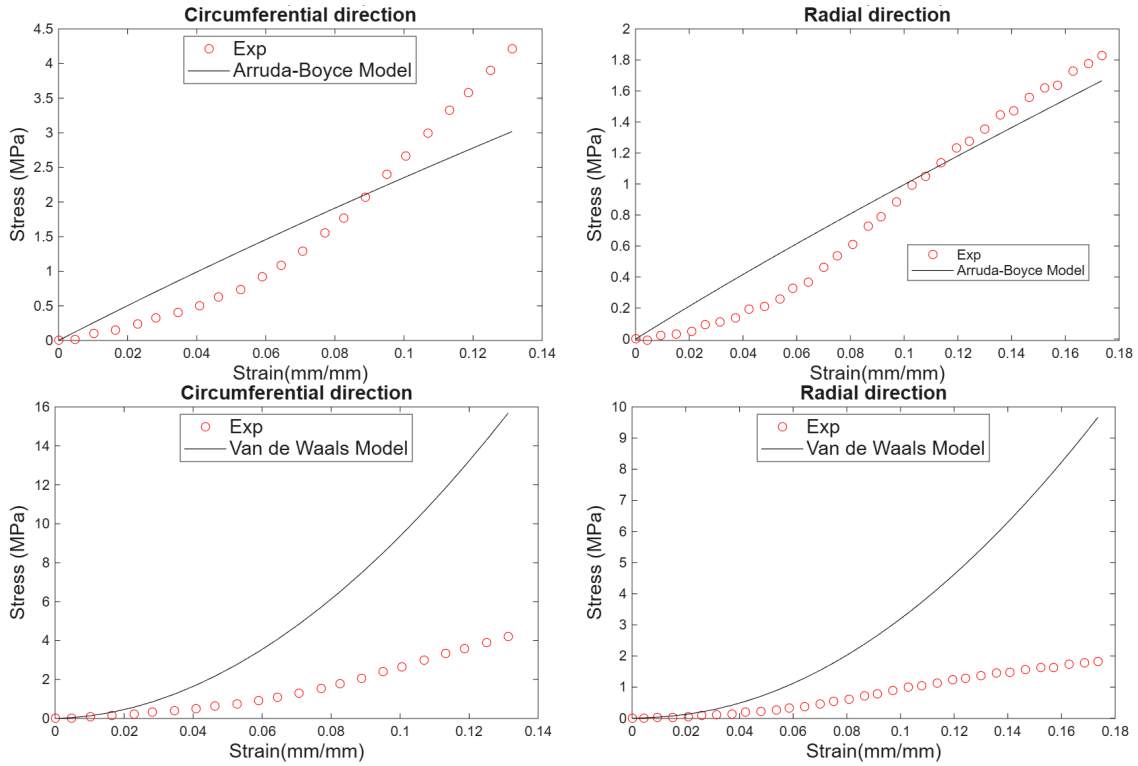



**Figure 4.** Five constitutive models' average parameters are used to fit the average data in the circumferential and radial directions.

**Table 1.** Averaged material parameters and statistical indicators obtained by using the Klosner–Segal model, Van De Waals model, and Arudda–Boyce Model.

| Klosner–Segal Model | | | Van de Waals Model | | | Arruda–Boyce Model | | |
|---|---|---|---|---|---|---|---|---|
| | Radial Average | Circumferential Average | | Radial Average | Circumferential Average | | Radial Average | Circumferential Average |
| **Sum of squares of diff** | 3.842566 | 5.631589 | Sum of squares of diff | 18.65423 | 15.75 | Sum of squares of diff | 103.7071 | 132.7611 |
| **Sum of Abs diff** | 16.90908 | 14.74341 | Sum of Abs diff | 36.1806 | 23.26 | Sum of Abs diff | 91.75289 | 74.80122 |
| **Normalized error** | 0.065748 | 0.065421 | Normalized error | 0.101417 | 0.09 | Normalized error | 0.321529 | 0.306431 |
| **NRMSE** | 0.07811 | 0.077177 | NRMSE | 0.123236 | 0.10 | NRMSE | 0.366444 | 0.348913 |
| **Correlation coefficient** | 0.996632 | 0.996413 | Correlation coefficient | 0.994901 | 0.99 | Correlation coefficient | 0.966854 | 0.967707 |
| **R2** | 0.992705 | 0.99204 | R2 | 0.985388 | 0.99 | R2 | 0.870062 | 0.853114 |
| **c11** | 0.78222 | 2.47671 | mu | 0.894007 | 1.20 | mu | 1.587221 | 6.133359 |
| **c21** | −0.25571 | −1.45354 | lamda_L | 11.86201 | 26.58 | lamda_L | 1 | 1.565474 |
| **c22** | 10.84298 | 31.99134 | a | −16.5545 | −220.24 | | | |
| **c23** | 0.856271 | −27.9898 | beta | −32.6722 | −0.45 | | | |

**Table 2.** Averaged material parameters and statistical indicators obtained using the Yeoh and Ogden Models.

| Yeoh Model | | | Ogden Model | | |
|---|---|---|---|---|---|
| | Radial Average | Circumferential Average | | Radial Average | Circumferential Average |
| **Sum of squares of diff** | 5.685031 | 6.989813 | Sum of squares of diff | 23.96937 | 15.7208 |
| **Sum of Abs diff** | 20.55151 | 15.59497 | Sum of Abs diff | 44.63508 | 24.36246 |
| **Normalized error** | 0.0721 | 0.062329 | Normalized error | 0.138817 | 0.10284 |
| **NRMSE** | 0.084646 | 0.073391 | NRMSE | 0.163124 | 0.122726 |
| **Correlation coefficient** | 0.996705 | 0.99628 | Correlation coefficient | 0.988069 | 0.991973 |
| **R2** | 0.992666 | 0.991876 | R2 | 0.971534 | 0.979784 |
| **c10** | 0.639166 | 1.299007 | mu1 | 0.265537 | 1.187777 |
| **c20** | 9.622904 | 24.44842 | alpha1 | 6.676369 | 1.028973 |
| **c30** | −0.35765 | −24.3257 | mu2 | 0.595033 | 1.819032 |
| | | | alpha2 | 0.458831 | 6.669015 |
| | | | mu3 | 0.773023 | 0.283513 |
| | | | alpha3 | 4.596073 | 5.114077 |

https://doi.org/10.3390/materproc2026031023

## 4. Discussion

The uniaxial properties of landrace pig pericardium are important, as they allow us to fully understand the mechanical properties of the landrace pig's pericardium and further synthesize it to be used as a durable, biocompatible, advanced hemodynamic and tissue-engineered scaffold for prosthetic aortic valve fabrication [27]. Uniaxial tests were performed till rupture to evaluate the maximum force at rupture, the maximum deformation at rupture, and Young's modulus of landrace pig's pericardium in the circumferential and radial directions independently [28]. To simulate the material's behavior under uniaxial testing and validate a finite element model to mimic experimental response, five isotropic constitutive models were selected and compared to see which models performed better and can be used for finite element analysis [29].

After preconditioning samples using ten cycles at a strain rate of 0.005/s, rupture tests were performed at a different strain rate of 0.1/s using a Cellscale biotester machine. Different strain rates affect the material response when subjected to different loading conditions, which include (but are not limited to) uniaxial loading [30]. The samples in the radial direction recorded a maximum stress of 8.569167 $\pm$ 1.808626 MPa, which is below the maximum applicable force of 23 N on a Cellscale biotester machine.

For the circumferential direction, three specimens ruptured just below the maximum applicable force of 23 N, and the other three did not rupture because, to effectively rupture the specimen, more force was required but could not be applied by the machine. The average maximum applied stress in the circumferential direction was 11.6695 $\pm$ 0.329884 MPa, which limits the accuracy of the averaged rupture strain and stress obtained in the circumferential direction, suggesting that either the strain rate could have been increased, which would not mimic physiological conditions, or a machine with a higher maximum force could have been used.

When comparing the strain or deformation of the specimen in the circumferential direction to the radial direction, the circumferential direction was more resistant to the applied stain, which required more force to elongate it, and the radial direction was compliant and strained more under lower applied forces; the same results were observed in [28]. The machine was only capable of applying a maximum force of 23 N, and thus was only capable of causing an average strain of 26% in the circumferential direction, which was not sufficient to rupture the specimen under the applied strain rate; similar issues were reported in [31]. The rupture strain in the radial direction was averaged at 56% strain. The 56% average strain was similar to that reported in [32], where the strain at rupture was approximately 60%. However, the stress at rupture was different from the stress at rupture or ultimate tensile stress (UTS) reported in this study, in which the UTS for the circumferential direction was found to be averaged at around 12 MPa, which is similar to the findings reported in [31–35]. The UTS was found to be doubled, and this could have been influenced by the strain rate, testing temperature, and the initial specimen's length and, most importantly, the fact that some samples did not rupture. The radial direction UTS was averaged at 8.5 MPa, which is comparable to the findings reported in [33,36]. Young's modulus in the circumferential direction was significantly larger than Young's modulus in the radial direction, suggesting that the specimen is anisotropic and hyperelastic, and the Young's modulus found in this study in the circumferential direction was 61.186742 $\pm$ 12.351925 MPa, which is similar to the findings in [31,34]; meanwhile, 71.59 $\pm$ 27.20 MPa was reported in [32,33] showed 100 MPa for this direction. The Young's modulus of native tissue was found to decrease as the material was crosslinked according to [37]. However, this was done for bovine pericardium. After choosing isotropic constitutive models for simplicity during the simulation, two constitutive models, namely the Klosner–Segal and Yeoh models, performed better than other models, and the material parameters found using these two

models can be used to simulate uniaxial tests of the pericardium. To properly evaluate the response of landrace pig pericardium, it is recommended to use biaxial or multiaxial loading methods, since the aortic valve undergoes loading in different directions in vivo. However, it is still important to evaluate independent material behavior when it is loaded in one direction.

## 5. Conclusions

Pericardia are used as materials to build prosthetic aortic valves without clearly understanding their mechanical properties, which limits the development of idealized synthesized landrace pig pericardium for the fabrication of optimized prosthetic aortic valves. After performing uniaxial tests, it was found that the landrace pig's pericardium is an anisotropic hyperelastic material, like most soft tissues. It was confirmed by observations that lower stresses were required to stretch the tissue by the same length along the radial direction than along the circumferential direction, suggesting that the radial direction was more compliant with the applied stress than the circumferential direction. Greater deformations were observed in the radial direction than in the circumferential directions, and the Young's modulus in the circumferential direction was significantly larger than in the radial direction. Five isotropic hyperelastic constitutive models were chosen for simplicity and to find the optimum material parameters to simulate uniaxial loading. Selecting all available isotropic hyperelastic constitutive models is impractical, and selecting three popularly used and two that are not popularly used could be a limiting factor, but it was found to be effective because two of the selected models fitted the experimental data well after the average material parameters were obtained from each experiment. Two of the constitutive models that produced superior results were the Klosner–Segal and Yeoh models, and these can be used in commercial finite element software to simulate the uniaxial load of the specimen. Methods used to synthesize native porcine pericardium should be optimized in such a way that the Young's modulus of the material is not highly deteriorated and the ultimate tensile strain is enhanced for the material to potentially have a prolonged lifespan.

**Author Contributions:** Conceptualization, F.N. and T.P.; methodology, H.M.N.; software, A.G.K.; validation, T.P., F.N. and H.M.N.; formal analysis, E.M.; investigation, E.M.; resources, T.P.; data curation, E.M.; writing—original draft preparation, E.M.; writing—review and editing, E.M.; visualization, E.M.; supervision, H.M.N.; project administration, T.P.; funding acquisition, T.P. All authors have read and agreed to the published version of the manuscript.

**Funding:** This research received no external funding.

**Institutional Review Board Statement:** The study was approved by the Ethics Committee of College of Agriculture and Environmental Sciences (Animal REC on 9 January 2025).

**Informed Consent Statement:** Not applicable.

**Data Availability Statement:** Data will be provided upon request.

**Acknowledgments:** Edward Matjeka would like to thank his parents for their ongoing financial and emotional support. Edward Matjeka would like to thank the University of South Africa Mechanical, Bioresources and Biomedical Engineering laboratory staff, and the employees and owners of the local abattoir for supplying us with samples.

**Conflicts of Interest:** The authors declare no conflict of interest.

## References


1. Thourani, V.H.; Puskas, J.D.; Griffith, B.; Svensson, L.G.; Pibarot, P.; Borger, M.A.; Heimansohn, D.; Beaver, T.; Blackstone, E.H.; Antonio, A.L.M.; et al. Five-year comparison of clinical and echocardiographic outcomes of pure aortic stenosis with pure aortic regurgitation or mixed aortic valve disease in the COMMENCE trial. *JTCVS Open* **2024**, *22*, 160–173. [CrossRef]
2. Henrique Rangel, R.; Voran, J.C.; Seoudy, H.; Villinger, T.; Lutter, G.; Puehler, T.; Kreidel, F.; Frank, J.; Salem, M.; Frank, D.; et al. Transcatheter aortic valve replacement in patients with severe aortic valve stenosis and concomitant mitral valve regurgitation—5 years follow-up. *IJC Heart Vasc.* **2024**, *53*, 101416. [CrossRef]
3. Thiene, G.; Rizzo, S.; Basso, C. Bicuspid aortic valve: The most frequent and not so benign congenital heart disease. *Cardiovasc. Pathol.* **2024**, *70*, 107604. [CrossRef]
4. Moawad, K.R.; Mohamed, S.; Hammad, A.; Barker, T. The Clinical Impact of Paravalvular Leaks with Transcutaneous Aortic Valve Implantation (TAVI) Versus Surgical Aortic Valve Replacement (SAVR): A Systematic Review and Meta-Analysis. *Heart Lung Circ.* **2024**, *33*, 1319–1330. [CrossRef] [PubMed]
5. Watkins, A.R.; El-Andari, R.; Fialka, N.M.; Kang, J.J.; Hong, Y.; Bozso, S.J.; Jonker, D.; Moon, M.; Nagendran, J.; Nagendran, J. Long-term outcomes following aortic valve replacement in bioprosthetic vs mechanical valves. *Heart Lung* **2025**, *69*, 87–93. [CrossRef] [PubMed]
6. Zhang, Z.; Han, R.; Huang, C.; Liu, Y.; Wang, G.; Bai, Y.; Yang, R.; Jin, T.; Zhang, X. Anisotropic electrospun poly(ε-caprolactone)/polycarbonate urethane scaffolds with improved fatigue performance for tissue-engineered heart valves. *Mater. Des.* **2025**, *259*, 114762. [CrossRef]
7. Madheswaran, D.K.; Ganesamoorthy, R.; Selvi, S.; Vezhavendhan, R.; Ravi, R.; Suresh, G.; Chandramohan, P. An assessment of additive manufacturing technology for automotive and aerospace applications. *AIP Conf. Proc.* **2024**, *3122*, 100012. [CrossRef]
8. Kotteesvaran, B.; Vijayakumar, S.; Suresh, G.; Vimalanathan, P. A review on: Technologists interest on natural fibers. *AIP Conf. Proc.* **2024**, *3122*, 100026. [CrossRef]
9. Stephen Bernard, S.; Vivek, S.; Suresh, G.; Kannan, G.K. Influence of 3-(8,11,14-Pentadecatrienyl) Phenol Cardanol as a Bio-Based Binder in a Brake Pad. In *Advances in Design and Thermal Systems; Lecture Notes in Mechanical Engineering*; Springer: Singapore, 2021; pp. 519–527. [CrossRef]
10. Nemavhola, F. Biaxial quantification of passive porcine myocardium elastic properties by region. *Eng. Solid Mech.* **2017**, *5*, 155–166. [CrossRef]
11. Ngwangwa, H.M.; Lebea, L.; Nemavhola, F.; Pandelani, T.; Modungwa, D. Investigation of the performance of different constitutive models on omasum uniaxial tensile behaviour. In *Current Perspectives and New Directions in Mechanics, Modelling and Design of Structural Systems—Proceedings of the 8th International Conference on Structural Engineering, Mechanics and Computation*; CRC Press/Balkema: Leiden, The Netherlands, 2022; pp. 349–353. [CrossRef]
12. Srinivasan, T.; Ramu, P.; Suresh, G.; Govardhan, Y.S.; Srinivasan, S. Impact of mechanical properties on sheet metal forming processes by using single-point incremental shaping method. *IOP Conf. Ser. Mater. Sci. Eng.* **2020**, *954*, 012028. [CrossRef]
13. Ngwangwa, H.M.; Semakane, L.; Nemavhola, F.; Pandelani, T.; Modungwa, D. Modelling of biaxial tensile behaviour of the tracheal tissue using three exponential-based hyperelastic constitutive models. In *Current Perspectives and New Directions in Mechanics, Modelling and Design of Structural Systems—Proceedings of the 8th International Conference on Structural Engineering, Mechanics and Computation*; CRC Press/Balkema: Leiden, The Netherlands, 2022; pp. 339–343. [CrossRef]
14. Suresh, G.; Jayakumari, L.S.; Dinesh Kumar, S. Finite element analysis of IPN reinforced woven fabric composite. *Rev. Mater.* **2017**, *22*, e-11882. [CrossRef]
15. Islam, T.; Uddin, M.W.; Uddin, R. Finite element analysis of motorcycle suspension system stability using different materials. *J. Eng. Res.* **2025**, *13*, 1230–1240. [CrossRef]
16. Nemavhola, F. Detailed structural assessment of healthy interventricular septum in the presence of remodeling infarct in the free wall—A finite element model. *Heliyon* **2019**, *5*, e01841. [CrossRef]
17. Ngwangwa, H.M.; Msibi, M.; Mabuda, I.; Nemavhola, F. Evaluating computational performances of Yeoh, Veronda-Westmann and Humphrey models on supraspinatus tendon uniaxial stress-strain behaviour. In *Current Perspectives and New Directions in Mechanics, Modelling and Design of Structural Systems—Proceedings of the 8th International Conference on Structural Engineering, Mechanics and Computation*; CRC Press/Balkema: Leiden, The Netherlands, 2022; pp. 354–358. [CrossRef]
18. Srinivasan, T.; Suresh, G.; Ramu, P.; Vignesh, R.; Harshan, A.V.; Vignesh, K.P. Effect of hygrothermal ageing on the compressive behavior of glass fiber reinforced IPN composite pipes. *Mater. Today Proc.* **2021**, *45*, 1354–1359. [CrossRef]
19. Priya, K.; Kumar, K.R.; Suresh, G.; Ganesamoorthy, R.; Ravi, R.; Chinnathambi Muthukaruppan, M. Analyzing the Fatigue Behaviour of E-Glass Fiber Reinforced Interpenetrating Polymer Networks (EP/VP/EV) Leaf Spring. *Mater. Sci. Forum* **2022**, *1065*, 35–45. [CrossRef]
20. Suresh, G.; Jayakumari, L.S. Evaluating the mechanical properties of E-Glass fiber/carbon fiber reinforced interpenetrating polymer networks. *Polimeros* **2015**, *25*, 49–57. [CrossRef]

21. Yap, C.H.; Saikrishnan, N.; Tamilselvan, G.; Yoganathan, A.P. Experimental measurement of dynamic fluid shear stress on the aortic surface of the aortic valve leaflet. *Biomech. Model. Mechanobiol.* **2012**, *11*, 171–182. [CrossRef] [PubMed]
22. Bourgin, P.; Cormeau, I.; Saint-Matin, T. A first step towards the modelling of the thermoforming of plastic sheets. *J. Mater. Process. Technol.* **1995**, *54*, 1–11. [CrossRef]
23. St. Pierre, S.R.; Linka, K.; Kuhl, E. Principal-stretch-based constitutive neural networks autonomously discover a subclass of Ogden models for human brain tissue. *Brain Multiphys.* **2023**, *4*, 100066. [CrossRef]
24. He, H.; Zhang, Q.; Zhang, Y.; Chen, J.; Zhang, L.; Li, F. A comparative study of 85 hyperelastic constitutive models for both unfilled rubber and highly filled rubber nanocomposite material. *Nano Mater. Sci.* **2022**, *4*, 64–82. [CrossRef]
25. Li, C.; Huang, X.; Zhang, L.; Hong, J.; Zhang, L.; Zhou, F. Constitutive modeling and seismic isolation performance of polyurethane-based tunnel isolation materials based on a modified Yeoh model. *Constr. Build. Mater.* **2025**, *496*, 143772. [CrossRef]
26. Chen, H.; Ou, J.; Li, H.; Peng, H.; Zhao, P.; Xiao, J. Composite dual-conical indentation model for obtaining the hyperelastic constitutive curves of rubber-like materials. *Polym. Test.* **2025**, *151*, 108968. [CrossRef]
27. Campion, G.; Hershberger, K.; Whelan, A.; Conroy, J.; Lally, C.; Murphy, B.P. A Biomechanical and Microstructural Analysis of Bovine and Porcine Pericardium for Use in Bioprosthetic Heart Valves. *Struct. Heart* **2021**, *5*, 486–496. [CrossRef]
28. Caballero, A.; Sulejmani, F.; Martin, C.; Pham, T.; Sun, W. Evaluation of transcatheter heart valve biomaterials: Biomechanical characterization of bovine and porcine pericardium. *J. Mech. Behav. Biomed. Mater.* **2017**, *75*, 486–494. [CrossRef]
29. Nemavhola, F. Study of biaxial mechanical properties of the passive pig heart: Material characterisation and categorisation of regional differences. *Int. J. Mech. Mater. Eng.* **2021**, *16*, 6. [CrossRef]
30. Noble, C.; Kamykowski, M.; Lerman, A.; Young, M. Rate-dependent and relaxation properties of porcine aortic heart valve biomaterials. *IEEE Open J. Eng. Med. Biol.* **2020**, *1*, 197–202. [CrossRef]
31. Zouhair, S.; Dal Sasso, E.; Tuladhar, S.R.; Fidalgo, C.; Vedovelli, L.; Filippi, A.; Borile, G.; Bagno, A.; Marchesan, M.; De Rossi, G.; et al. A comprehensive comparison of bovine and porcine decellularized pericardia: New insights for surgical applications. *Biomolecules* **2020**, *10*, 371. [CrossRef]
32. Bagno, A.; Aguiari, P.; Fiorese, M.; Iop, L.; Spina, M.; Gerosa, G. Native Bovine and Porcine Pericardia Respond to Load with Additive Recruitment of Collagen Fibers. *Artif. Organs* **2018**, *42*, 540–548. [CrossRef]
33. Gauvin, R.; Marinov, G.; Mehri, Y.; Klein, J.; Li, B.; Larouche, D.; Guzman, R.; Zhang, Z.; Germain, L.; Guidoin, R.; et al. A comparative study of bovine and porcine pericardium to highlight their potential advantages to manufacture percutaneous cardiovascular implants. *J. Biomater. Appl.* **2013**, *28*, 552–565. [CrossRef]
34. Dong, J.; Li, Y.; Mo, X. The study of a new detergent (octyl-glucopyranoside) for decellularizing porcine pericardium as tissue engineering scaffold. *J. Surg. Res.* **2013**, *183*, 56–67. [CrossRef] [PubMed]
35. Choe, J.A.; Jana, S.; Tefft, B.J.; Hennessy, R.S.; Go, J.; Morse, D.; Lerman, A.; Young, M.D. Biomaterial characterization of off-the-shelf decellularized porcine pericardial tissue for use in prosthetic valvular applications. *J. Tissue Eng. Regen. Med.* **2018**, *12*, 1608–1620. [CrossRef] [PubMed]
36. Arbeiter, D.; Grabow, N.; Wessarges, Y.; Sternberg, K.; Schmitz, K.P. Suitability of porcine pericardial tissue for heart valve engineering: Biomechanical properties. *Biomed. Tech.* **2012**, *57*, 882–883. [CrossRef]
37. Hülsmann, J.; Grün, K.; El Amouri, S.; Barth, M.; Hornung, K.; Holzfuß, C.; Lichtenberg, A.; Akhyari, P. Transplantation material bovine pericardium: Biomechanical and immunogenic characteristics after decellularization vs. glutaraldehyde-fixing. *Xenotransplantation* **2012**, *19*, 286–297. [CrossRef] [PubMed]


**Disclaimer/Publisher's Note:** The statements, opinions and data contained in all publications are solely those of the individual author(s) and contributor(s) and not of MDPI and/or the editor(s). MDPI and/or the editor(s) disclaim responsibility for any injury to people or property resulting from any ideas, methods, instructions or products referred to in the content.